Propagation of a laser-driven relativistic electron beam inside a solid dielectric

G. S. Sarkisov

Raytheon Ktech, 1300 Eubank Blvd, Albuquerque, New Mexico, 87123, USA

V. V. Ivanov, P. Leblanc, Y. Sentoku, K. Yates, P. Wiewior, O. Chalyy, and A. Astanovitskiy
Department of Physics, University of Nevada Reno, 5625 Fox Ave, Reno, Nevada, 89506, USA

V. Yu. Bychenkov

P.N. Lebedev Physics Institute, RAS, 53 Leninski Prospect, Moscow, 119991, Russia

D. Jobe and R. B. Spielman
Raytheon Ktech, 1300 Eubank Blvd, Albuquerque, New Mexico, 87123, USA

Laser probe diagnostics: shadowgraphy, interferometry, and polarimetry were used for a comprehensive characterization of ionization wave dynamics inside a glass target induced by a laser-driven, relativistic electron beam. Experiments were done using the 50-TW Leopard laser at the University of Nevada, Reno. We show that for a laser flux of $\sim 2 \times 10^{18}$ W/cm^2 a hemispherical ionization wave propagates at c/3 for 10 ps and has a smooth electron-density distribution. The maximum free-electron density inside the glass target is $\sim 2 \times 10^{19}$ cm^{-3}, which corresponds to an ionization level of $\sim 0.1\%$. Magnetic fields and electric fields do not exceed ~ 15 kG and ~ 1 MV/cm, respectively. The electron temperature has a hot, ringlike structure with a maximum of ~ 0.7 eV. The topology of the interference phase shift shows the signature of the "fountain effect", a narrow electron beam that fans out from the propagation axis and heads back to the target surface. Two-dimensional particle-in-cell (PIC) computer simulations demonstrate radial spreading of fast electrons by self-consistent electrostatic fields driven by laser. The very low ionization observed after the laser heating pulse suggests a fast recombination on the sub-ps time scale.

I. INTRODUCTION

Developments in short-pulse, high-intensity lasers make it possible to efficiently generate electrons in interactions with solid targets. However, fast-electron propagation and energy deposition in solid-density matter, especially in insulators, still require comprehensive study, although several steps in this direction have already been taken. Such studies may have an impact on laser-based electron accelerators with foils [1], fast igniter approaches to inertial confinement fusion [2], electron radiography [3], hard x-ray sources [4], etc. Both fundamental and applied studies may benefit from a comprehensive understanding of fast-electron propagation in solid matter.

An important issue in electron transport is the inhibition of electron transport by strong ambipolar electric fields unless those fields are neutralized by a return current of the background free electrons or electrons appearing as a result of ionization [5–7]. This effect depends on material conductivity and is especially complicated in dielectrics. The effect of the electric field, which depends on electron penetration depth, defines whether ion acceleration occurs from the target front surface or from the backside of the target [8]. The first indirect experimental indications of electric field effects were reported in Refs. [9,10]. Experimental evidence of inhibition of fast-electron penetration in insulators was suggested in Ref. [11].

The formation of an ionization wave inside a glass target as result of an interaction with a short pulse laser (pulse duration $\tau = 100$ fs, wavelength $\lambda = 616$ nm) at low intensity I = 5×10^{14} W/cm^2, was observed by Vu *et al.* [12] by measuring the Doppler shift of the reflected probing beam. The reconstructed expansion velocity $v \sim 1.8 \times 10^7$ cm/s was explained by standard electron-thermal conduction model. The first observation of a laser-driven ionization wave inside a glass target at high laser intensity (I = 10^{17} W/cm^2, $\tau = 2$ ps, $\lambda = 1054$ nm), using single-frame shadowgraphy was reported by Ditmire *et al.* [13]. They showed that the ionization wave expands hemispherically at a velocity of $v \sim 8 \times 10^8$ cm/s up to ~ 0.1 mm inside the glass target, which is consistent with radiation-driven thermal transport. Shadowgraphy of fast electrons, driven by an ultra-intense laser pulse with I $\sim 10^{19}$ W/cm^2 ($\tau = 0.35$ ps, $\lambda = 530$ nm), was done inside a glass target by Gremillet *et al.* [14]. They showed the presence of narrow axial jets moving at a velocity nearing the speed of light c as well as the hemispherical ionization expanding with velocity $\sim c/2$. Because the experimental techniques in Refs. [13,14] were restricted to single-frame shadowgraphy, there is a lack of experimental data that is critical to better understand the physics of laser-glass interactions.

The propagation of a laser-produced electron beam through an insulator was investigated using a one-dimensional (1D) model, which describes ionization behind the beam front and defines the ionization-wave velocity in terms of characteristic electron energy and electron density [7]. A 3D hybrid code [14] was used to model the ionization expansion as quasineutralized diffusive plasma, neglecting the breakdown field in the dynamic ionization process. 1D particle-in-cell (PIC) simulations, with collisional and field ionization, were used to study the ionization wave in an insulator target in the

subrelativistic regime, where the diffusive thermal transport was dominant and the sheath field at the ionization front was lower than the breakdown field [15].

In this paper we show for the first time a comprehensive characterization of ionization wave dynamics inside a solid-state glass target induced by a laser-driven, relativistic electron beam. Experimental results show the hemispherical propagation of an ionization wave inside the glass at $c/3$. The maximum ionization of the glass is as large as 0.1%. The front of the ionization wave has a smooth edge and is semitransparent to the green probe beam. Polarimetry shows that the magnetic fields and the electric fields do not exceed values $\sim$15 kG and $\sim$1 MV/cm. The maximum electron temperature inside glass target is $\sim$0.7 eV. The topology of the wave-front disturbances shows the signature of the "fountain effect" of fast electrons inside solid target. Interferometry shows abrupt axial maxima of electron density. 2D PIC simulations demonstrate the dynamics of the ionization wave in the breakdown regime. They show the electrostatic inhibition of the fast current at the insulator-plasma interface and quasistatic magnetic-field excitation at the ionization front. A condensed version of our primary results was published in Ref. [16].

II. EXPERIMENT

The experiment was performed with the 50-TW Leopard laser facility at the University of Nevada, Reno [17]: $\lambda = 1057$ nm, $\tau \approx 0.4$ ps, 10^6-intensity contrast ratio at $\sim$1 ns, 1.4-J to 10-J beam energy, 15-μm focal spot size, I = 2 $\times$ $10^{18} - 1.4 \times 10^{19}$ W/cm^2, and a f/2 parabolic mirror. A BK7 glass slide of 1.1-mm thickness was used as the target. Two experimental setups were used for the investigation of ionization wave dynamics inside of the glass target: two-frame shadowgraphy-interferometry (two instants of time) and single-frame polarimetry-shadowgraphy-interferometry (one instant in time). We used 16-bit, 8-Mpixel cooled CCD cameras for recording images. The spatial resolution was $\sim$15 μm. The exposure time was $\sim$0.4 ps. The intensity of the probing laser was carefully reduced with ND filters to avoid a nonlinear interaction of the probe beam with the optics and the focal spot in the air.

A. Two-frame shadowgraphy-interferometry diagnostic

The experimental setup of the two-frame shadowgraphy-interferometry diagnostic is shown in Fig. 1. This diagnostic shows absorption and wave-front distortion images of the laser-glass interaction area for two moments in time. The second harmonic of the heating laser was used as the probe beam. This laser light was split into two probe beams each having orthogonal linear polarizations, equal intensities, and adjustable delay times. The two probe beams were angularly separated using a 3° calcite wedge to create two spatially separated shadowgrams in the first CCD camera. An air-wedge shearing interferometer [18] creates two spatially separated interferograms in the second CCD camera. To avoid overlapping the separated images, a visual diaphragm was used.

B. One-frame polarimetry, shadowgraphy, and interferometry diagnostic

The experimental setup of one-frame polarimetry-shadowgraphy-interferometry diagnostic is presented on Fig. 2. This diagnostic is used for reconstruction of the structure of the magnetic field, the electric field, the electron density, and the electron temperature inside the dielectric target at one instant in time using the induced anisotropy of the refractive coefficient of the glass, the wave front disturbance, and the absorption of the probe light. In this setup, the Glan prism polarizer creates high-contrast, linearly polarized light to probe the plasma. The collimator creates an image of the interaction region in the plane of the visual diaphragm. The F3 lens creates images of the interaction region with visual diaphragm into two CCD cameras. The 3° calcite wedge angularly splits the probing beam into two channels: the shadow channel (with almost all of the intensity) and the Faraday channel (with small intensity $\sim\sin^2$ of the decrossing angle). In our experiments we use a 6° decrossing angle. To create shadow and Faraday images in one CCD camera, we use a sheet polarizer to equalize the light intensities. A shearing air-wedge interferometer [18] creates an interferogram in a second CCD camera.
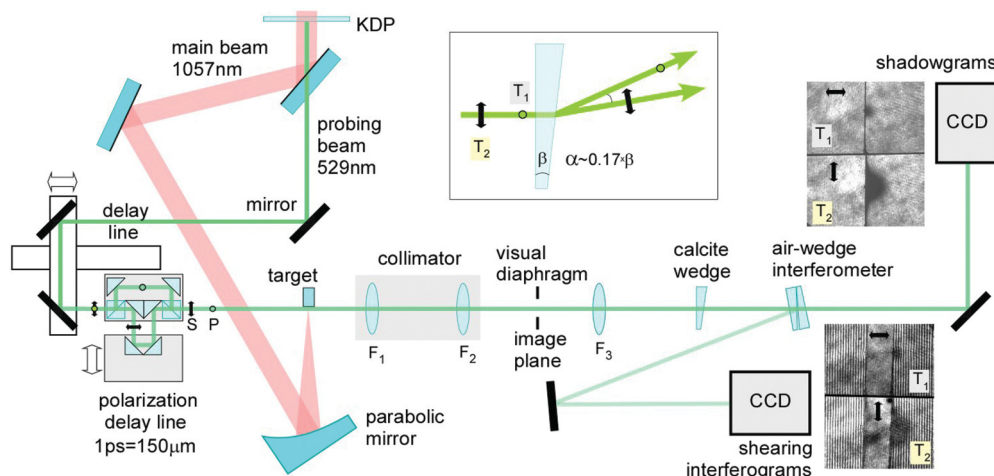
FIG. 1. (Color online) The two-frame shadowgraphy-interferometry diagnostic setup.
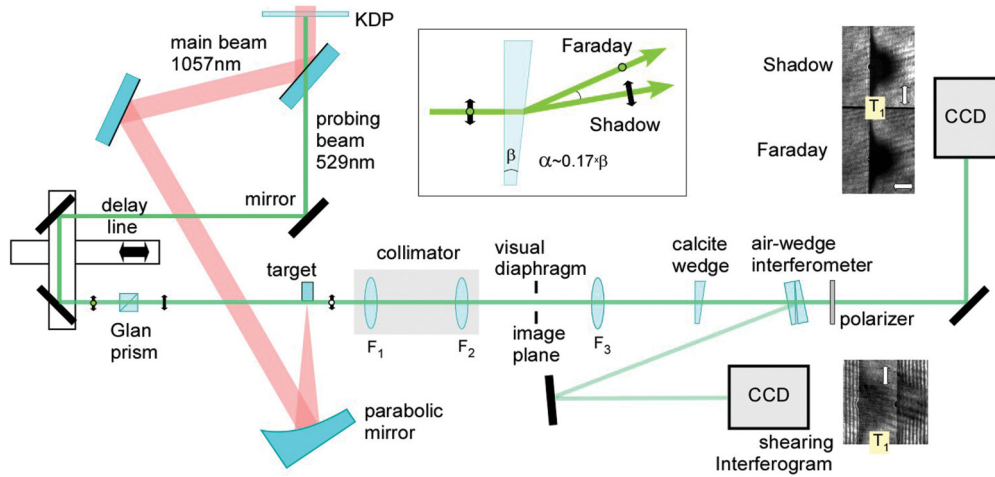
FIG. 2. (Color online) The one-frame, three-channel polarinterferometer setup.

C. Temporal alignment of the probe beam and the heating beam

The imaging of air breakdown in the focus of the heating laser was used for the temporal alignment of the probe and heating beams. Figure 3 shows shadows and interferograms of air breakdowns taken at different moments in time with a 1-ps interframe time (-2 ps; -1 ps; 0 ps; $+1$ ps; $+2$ ps). Images at -2 ps and -1 ps were taken during a single laser shot (as well as images at $+1$ ps and $+2$ ps). The laser energy was $\sim$100 mJ. In the shadowgrams we can see small ionization spots from the ns-long laser prepulse and a large ionization cone from the main sub-ps pulse. The double structure of these spots is related to the temporal structure of the laser prepulse. A large ionization cone propagates toward the focal plane of the laser. We can see obvious differences in the images: the interference fringes close to the focal plane have almost no disturbance for -2 ps, -1 ps, and 0 ps and a large disturbance at 1 ps and 2 ps. A zero delay between probe and heating beams corresponds to the observation of the first visible disturbance of the interference lines at the focal plane.

III. RESULTS

A set of experiments was conducted to investigate the propagation dynamics of the ionization wave, the electron density, and to estimate the magnetic field, electric field, and electron temperature inside the glass target.

A. Ionization wave dynamics

Figure 4 shows complementary shadowgrams and interferograms of the laser-glass interaction at 0 ps, 3.3 ps, 6.6 ps, 10 ps, and after-shot images. Vacuum is to the left of the vertical line and glass is to the right of the line. The shadowgrams show absorption hemispheres with smooth edges, which expand in time, and laser plasma expanding into the vacuum. It is obvious that the dark area in the glass side of the target is due to light absorption (there are no diffraction lines), while the vacuum side nontransparency with the laser plasma is due to refraction of the probe beam (there are diffraction lines there). Initially, plasma was produced at the glass-vacuum interface by the $\sim$1-ns laser prepulse with intensity $\sim10^{12}$ W/cm^2. Before the main pulse with intensity $\sim 2 \times 10^{18}$ W/cm^2 heated the target ($t = 0$) there was no absorption and no interference phase shift of the probing beam in the glass was observed. After the main pulse arrived, the absorption hemisphere appeared and expanded into the glass during $\sim$10 ps up to $\sim$750-μm depth with the maximum velocity of $c/3$ ($\sim$100 μm/ps). The final absorption image ($t = 10$ ps) remains the same for a long time, at least up to nanoseconds. Increasing the laser energy
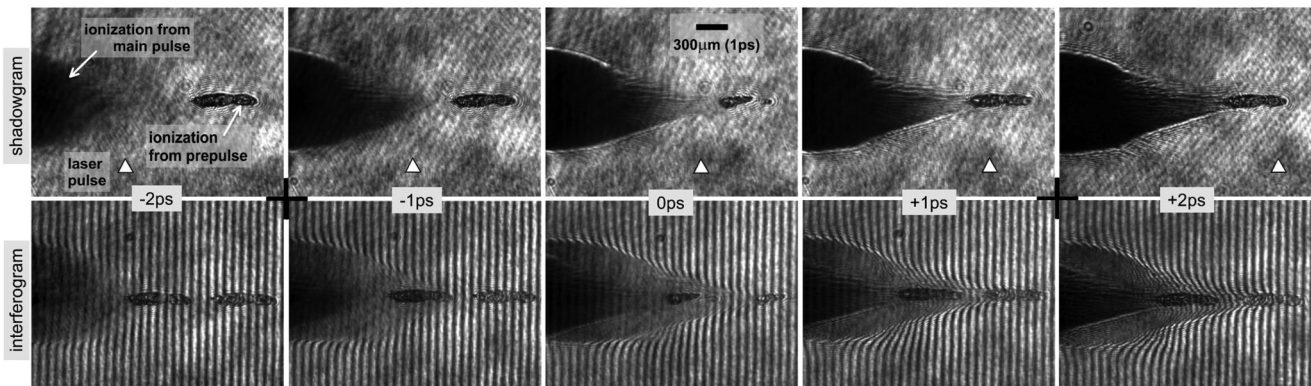
FIG. 3. Complementary shadowgrams and interferograms of air breakdown in a laser focus are shown at different moments in time.
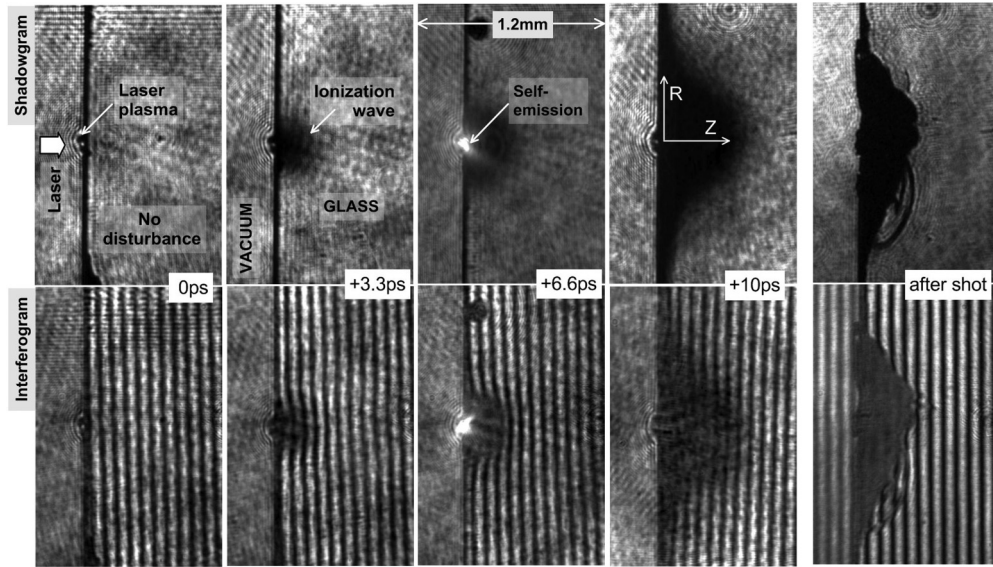
FIG. 4. Complementary shadowgrams and interferograms of the ionization wave inside the glass target are shown at different moments in time.

by five times (I $\sim 10^{19}$ W/cm^2) resulted in a modest increase in the ionization depth up to $\sim$1 mm, which is similar to the data in Ref. [14]. The interferograms in Fig. 4 demonstrate a significant disturbance of the probe wave front inside the glass. It is interesting that ionization hemispheres stayed the same for a long time while the interference phase shift disappeared. Probably this result from contribution of excited atoms: the positive sign of the excited atoms refractivity compensated for the negative refractivity of the free electrons. The size of the crater inside the glass target after the shot was correlated to maximum size of the ionization region ($t > 10$ ps) during the shot ($t = 10$ ps).

Figure 5 shows the axial profile of the light absorption taken from shadowgram at 3.3 ps. In this plot, we can see how we determine the axial edge of the light absorption. In this time,
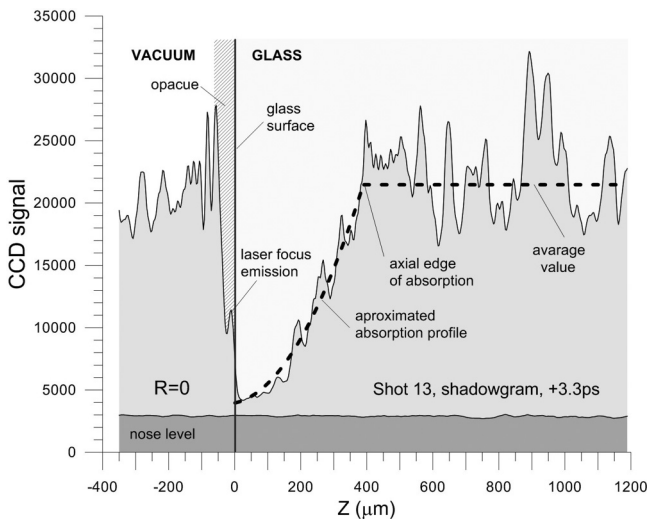
the maximum light absorption is above the noise level. There is no saturation of the light signal in the absorption area.

Figure 6(a) shows the dynamics of the axial position of the absorption depth for a laser flux I $\sim 2 \times 10^{18}$ W/cm^2 (we defined the edge as the place with a 10% light-intensity drop due to absorption). Also, we plot similar data for edge dynamics taken from Ref. [14] (LULI, I $\sim 1 \times 10^{19}$ W/cm^2, 532-nm wavelength, 0.3-ps pulse width, and 10^{10} contrast) and Ref. [13] (IC, I $\sim 1 \times 10^{16}$ W/cm^2, 1054-nm wavelength, 2-ps pulse width, and 10^6 contrast). For our experiments with I $\sim 2 \times 10^{18}$ W/cm^2 the absorption depth increased with an initial speed of $\sim$100 μm/s ($\sim$c/3) and stopped at $\sim$10 ps. For a laser flux I $\sim 1 \times 10^{19}$ W/cm^2 [14], the initial speed of absorption depth was $\sim$150 μm/s and reached a maximum penetration depth at $\sim$6 ps. For a laser flux I $\sim 10^{16}$ W/cm^2 [13] the initial speed of absorption depth was $\sim$7 μm/s and reached a maximum penetration depth at $\sim$12 ps. We saw that the expansion velocity and the penetration depth was flux dependent and for I $\sim 10^{18}$–10^{19} W/cm^2 the absorption depth expanded with nearly light-speed values $c/3$ to $c/2$.

Figure 6(b) demonstrates the maximum ionization penetration depth vs laser flux. For the smaller laser fluxes, I $\sim 10^{15}$ W/cm^2 to 10^{17} W/cm^2, the penetration depth can be approximated by linear function of flux. For larger laser fluxes, I $\sim 10^{17}$ W/cm^2 to 10^{19} W/cm^2, the penetration depth is a logarithmic function of flux. Our results fit well to low-intensity data from IC [13] and high-intensity data from LULI [14]. It is interesting that the propagation length is independent of laser wavelength (1057 nm in our experiments and 532 nm in Ref. [14]), the condition of the target surface (glass in our experiments and Al film in Ref. [14]), and the prepulse value (a contrast of 10^6 in our experiment and 10^{10} in Ref. [14]).

Figure 7 demonstrates maximum speed of the ionization wave vs the intensity-wavelength parameter $I \times \lambda^2$. The speed of the ionization monotonically increased with laser flux. We can see that low-intensity data from IC [13] and high-intensity data (UNR and LULI [14]) can be approximated by theoretical

FIG. 5. The axial absorption profile of the probe laser light is taken from the shadowgram at 3.3 ps.
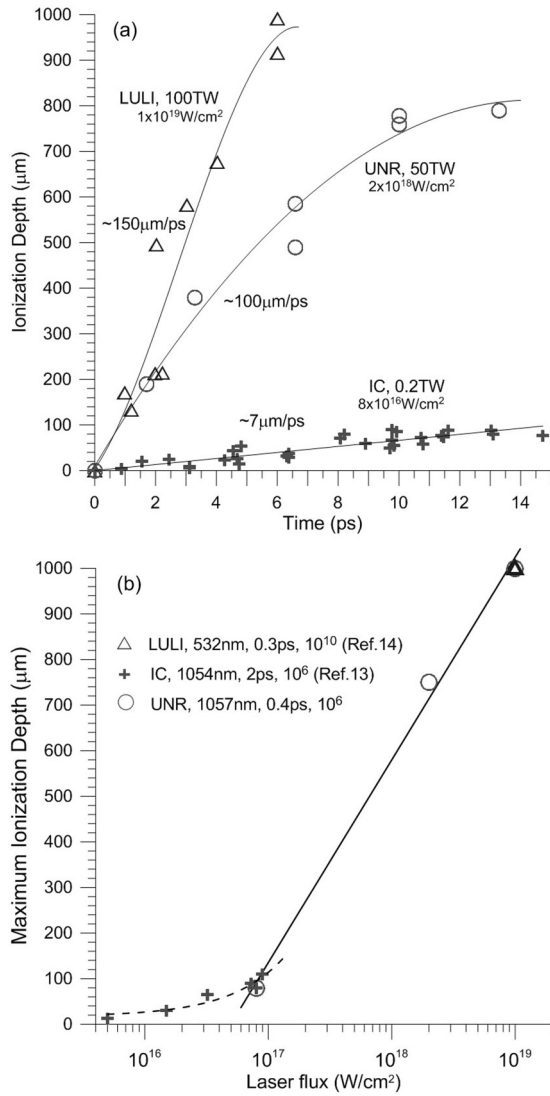
FIG. 6. (a) We plot the dynamics of the axial position of the ionization wave as a function of time inside the glass target. (b) The ionization wave penetration depth is plotted as a function of laser flux.

curve (solid line). We will discuss analytical approximation for ionization speed later in our paper.

B. Interference phase shift and electron density

Figure 8 shows profiles of the interference phase shift along the heating beam axis for the vacuum and the glass parts of the target and profiles of absorption at 3.3 ps. The laser intensity was $\sim 2 \times 10^{18}$ W/cm^2. The laser-plasma phase shift has only a negative sign corresponding to the free-electron refractivity. The disturbance inside the glass demonstrates first a negative and, later, a positive phase shift. It is obvious that the negative phase shift in the glass is due to free-electron refractivity, while the positive phase shift is due to the excited atom (bound electron) contribution. The axial length of the absorption profile inside the glass coincides with axial length of the negative free-electron part of interference phase shift. It is interesting that two independent diagnostics demonstrate similar a spatial scale of the ionization depth inside the glass.
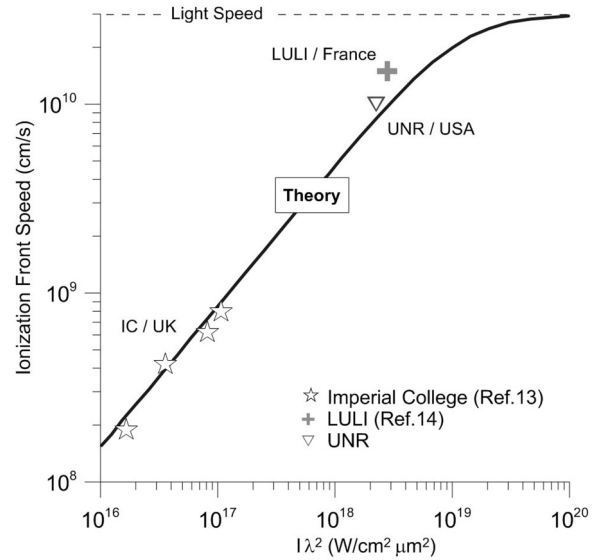
FIG. 7. The maximum speed of the ionization front is plotted as a function of the laser intensity-wavelength parameter.

A similar behavior of refraction was discussed in detail in Ref. [19].

Figure 9 shows the topology of the interference phase shift at the probe time, $t = 3.3$ps for the vacuum (laser plasma) and the glass (e-beam effect) parts of the target. The negative disturbance of the wave front from the vacuum side of the target is due to laser plasma expanding into the vacuum, created by the ns laser prepulse. A more complicated disturbance of the wave front (positive and negative) inside the glass target is related to electron beam effect. The undersurface part of wave-front disturbance corresponds to a negative phase shift from free electrons, while the periphery has a positive phase shift from excited atoms (bound electrons). This refractivity effect was demonstrated and discussed in detail for the gas-plasma stage of matter in Ref. [19]. We can see in Fig. 9 the radial split of the wave-front axial peak with distance from target surface. This behavior of integral phase shift can be explained only by spreading of local electron-density axial-peak with distance Z.

Figure 10 shows the radial distribution of the phase shift for $t = 1.7$ ps and $t = 3.3$ ps and the reconstructed local distribution of the electron density close to the vacuum-glass interface. It is very important that both electron-density n_e profiles have sharp and narrow (~ 40-μm half width) maxima $\sim 2.2 \times 10^{19}$ cm^{-3} on the axis ($R = 0$). This value for n_e gives a glass ionization estimate less than 0.1%. The sharp peak of electron density can be explained by the effect of the narrow electron beam generated in the laser focus propagating inside the glass.

C. Electron temperature estimate

The absorption and interference phase shifts of the probe laser beam can be used to estimate the free-electron temperature inside the glass target. For a weakly ionized plasma ($Z \ll 1$), the absorption coefficient depends on electron-atom collision frequency and can be written according to
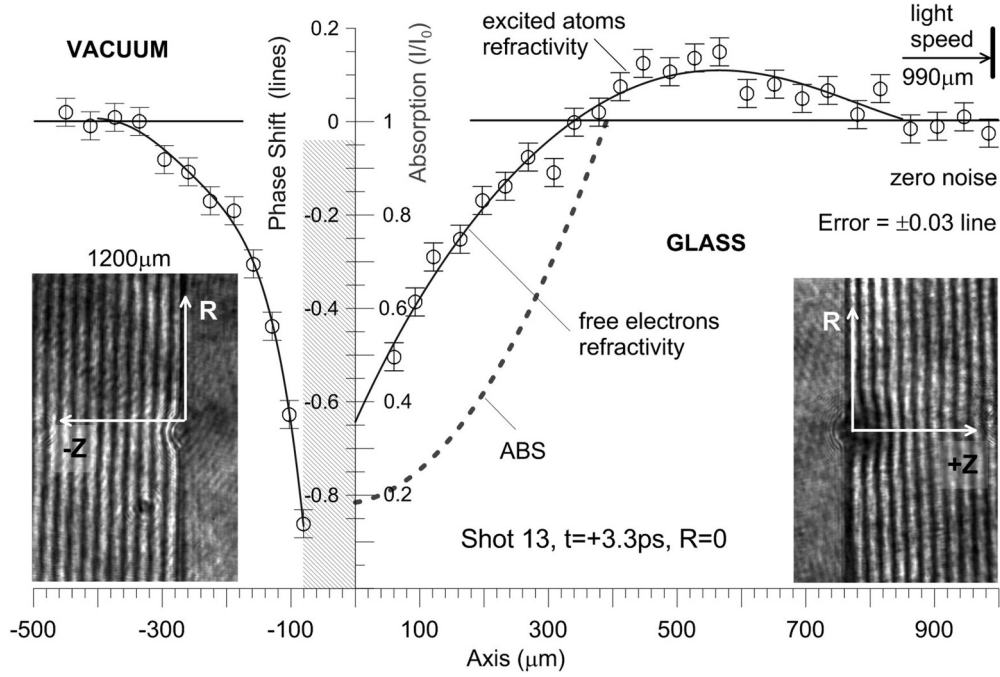
FIG. 8. We show the axial distributions of the interference phase shift and the absorption profile inside and outside the glass target.

well-known Drude model as

$$K[\text{cm}^{-1}] = \left(\frac{\omega_p}{\omega}\right)^2 \left(\frac{\nu_{\text{ea}}}{c\mu}\right)$$

$$= 1.25 \times 10^{-16} \lambda^2 \frac{n_e N_a \sigma(T)}{\mu \sqrt{1 - n_e/n_c}} \sqrt{T_e} \quad (1)$$

$$\nu_{\text{ea}}[s^{-1}] = 1.26 \times 10^{-6} m_e^{-1/2} N_A \sigma(T) \sqrt{T_e}$$

$$= 4.2 \times 10^7 N_A \sigma(T) \sqrt{T_e}, \quad (2)$$

where ν_{ea} is the electron-atom collision frequency in s^{-1}, λ is the wavelength in cm, N_A is the atomic density in cm^{-3} ($N_A = 3 \times 10^{22}$ cm^{-3} for BK-7), n_c is the critical electron density for wavelength λ, n_e is the electron density in cm^{-3}, m_e is the electron mass in g, $\sigma(T)$ is the electron-atom elastic collision cross section in cm^2 ($\sim 10^{-16}$ cm^2), T_e is the electron temperature in eV. It is important that Eq. (2) be valid for $\nu_{\text{ea}} \ll \omega$ (probing beam frequency). The refraction coefficient μ of the glass at 529 nm is 1.52.
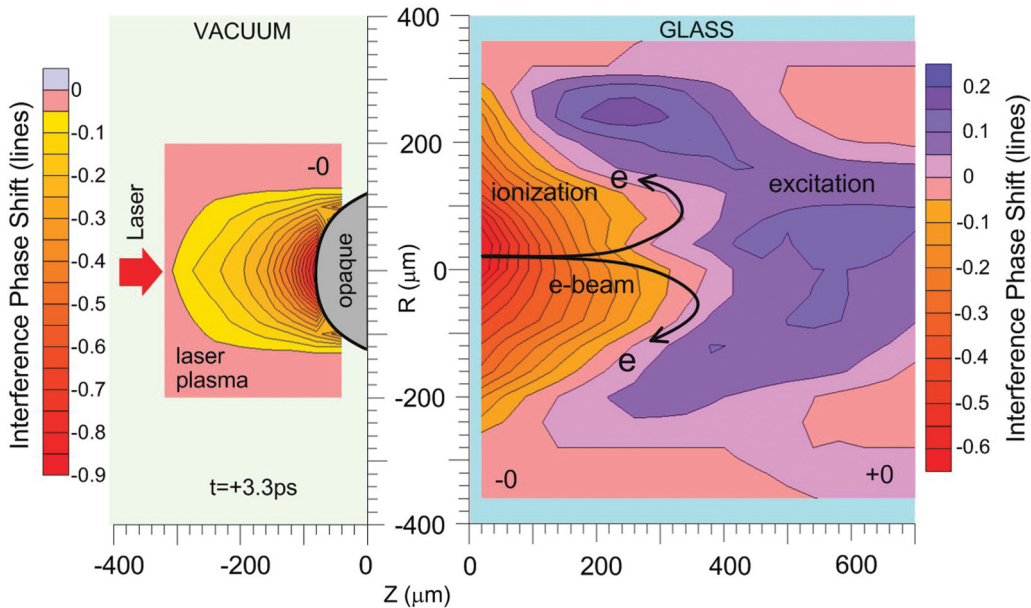
FIG. 9. (Color online) The topology of the ionization wave front at 3.3 ps for the vacuum and the glass side of the target.
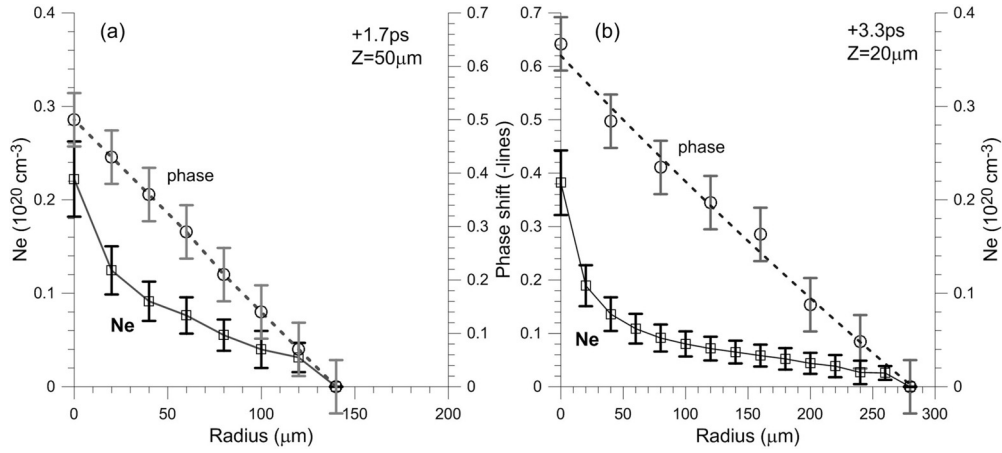
FIG. 10. The radial profiles of phase shift and electron density are plotted for (a) $t = 1.7$ ps and (b) 3.3 ps.

For an axial-symmetric medium $[K = K(r)$ and $n_e = n_e(r)]$, the final expression for electron temperature in eV is

$$T_e(r) = 6.4 \times 10^{31} \frac{(1 - n_e/n_c)}{\lambda^4 N_a^2} \mu^2 \left(\frac{K(r)}{n_e(r)} \right)^2 \sigma (T_e)^{-2}, \quad (3)$$

where K is in cm^{-1}, n_e, n_c, and N_a are in cm^{-3}, λ is in cm, $\sigma(T_e)$ is in cm^2. Local values of $K(r)$ and $n_e(r)$ can be recovered using an Abel inversion for experimental radial distributions of absorption and interference phase shift.

This absorption laser-probing technique was used for the measurement of electron temperature inside a highly ionized Z pinch in Ref. [20]. It is interesting that light absorption for high-ionized and low-ionized plasmas has an absolutely different behavior vs. temperature. For $Z > 1$, light absorption decreases with temperature as $T^{-3/2}$. For $Z \ll 1$, light absorption increases with temperature as $T^{1/2}$. For highly ionized plasmas, light absorption is significantly more sensitive to the magnitude of the electron density ($\sim n_e^2$ vs. $\sim n_e$).

Figure 11(a) shows the radially integrated profiles of light absorption (I/I_0) and the phase shift at 3.3 ps and at a distance 20 μm from glass surface. These integrated profiles

were used in reconstructions of the local distributions of the electron density, the absorption coefficients, and the electron temperature presented in Figure 11(b). The radial distribution of the electron temperature was plotted for two constant values of electron-atom elastic collision cross-section $\sigma = 10^{-16}$ cm^2 and 2×10^{-16} cm^2 and for energy-dependent cross-section $\sigma(T)$ for electron-atomic oxygen collisions [21]:

$$\sigma(T) = 10^{-16} \times (1.44 + 2.62T - 0.28T^2) \quad (4)$$

The electron temperature inside the glass demonstrates the existence of a "hot ring" with a maximum temperature in the range of 0.25 eV to 1.1 eV (average $\sim$0.7 eV) at a distance $\sim$80 μm from axis. The axial temperature is cold, $\sim$0.1 eV. It is interesting that the temperature profiles for $\sigma = 2 \times 10^{-16}$ cm^2 and $\sigma(T)$ almost coincide. The value of the temperatures at larger radii is unreliable because for $r > 200$ μm an Abel inversion here gives almost 100% error. The accuracy of our results could be significantly improved if we were to use tabulated, electron-atom low-energy elastic collision cross-sections for SiO_2. Currently these data are not available in the literature.
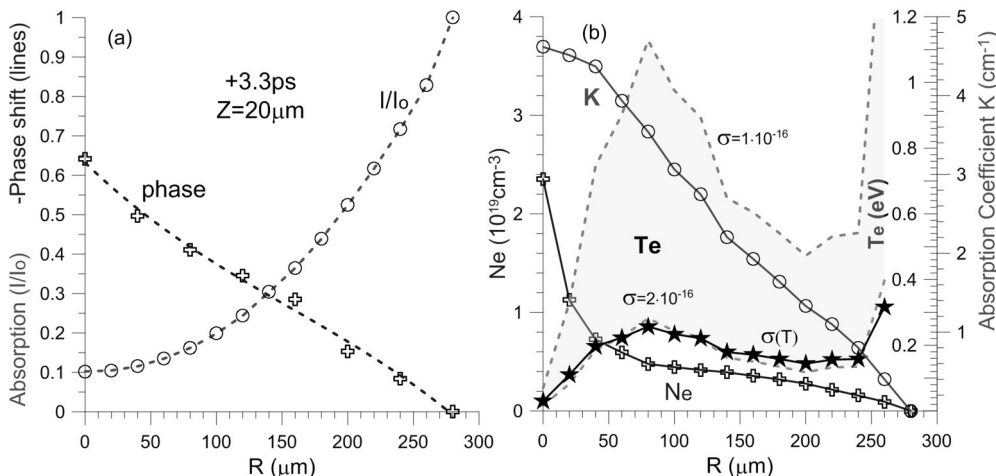
FIG. 11. (a) The absorption (I/I_0) & the phase shift; (b) the local distributions of electron density $N_e(r)$ (crosses) & absorption coefficient $K(r)$ (circles), and the electron temperature $T_e(r)$ (stars) are plotted as a function of radius.

D. Magnetic and electric field measurements

For measurements of magnetic fields and electric fields inside the glass target we used the magneto-optical Faraday Effect and the electro-optical Kerr Effect. A three-channel polar interferometer (Fig. 2) was used to measure the magnetic fields and the electric fields inside and outside the glass target. For the measurement of the fields inside the glass target, it is enough to use only 2-channel polarimetry (because Verdet and Kerr constants are available for the BK7 glass). For the measurements of the magnetic fields inside the laser plasma it is necessary to use 2-channel polarimetry and interferometry (for the measurements of electron density along the probe beam path). The magnetic field and electric field measurements are similar to those described for water discharges in [22] (Faraday effect) and in [23] (Kerr effect). This measurement technique was described in a detail in [24].

Figure 12 shows a set of Faraday, shadowgram and interferogram images of laser-glass interactions ($I \sim 2 \times 10^{18}$ W/cm^2) at 3.3 ps and 10 ps. The decrossing angle between the polarizer and the analyzer was $\alpha_0 = 6°$ (light penetration is minimal for $\alpha_0 = 0$). For all times during the measurement we saw no differences in the light intensity around the ionization area. This means that Faraday and Kerr effects are less than the detection threshold. We can estimate
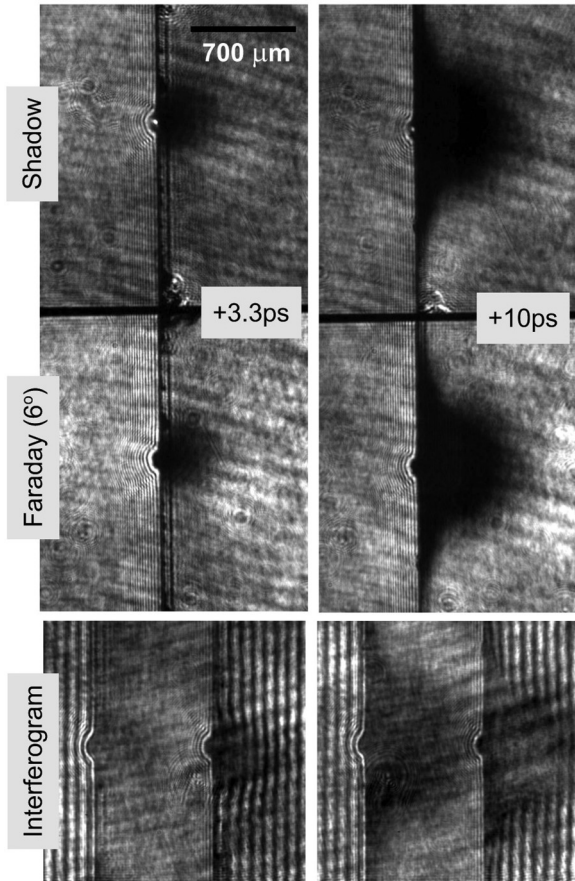
FIG. 12. The shadowgram, faraday (6°), and interferogram data of the ionization wave inside a BK7 glass target are shown at 3.3 ps and 10 ps.

this threshold for Faraday and Kerr effects for moment after 1.7 ps.

1. Faraday effect

The rotation angle in the polarization plane can be written as: $\alpha = VBL$, where V is the Verdet constant in deg/G/cm, B is the magnetic field in G and L is the path length in cm. For $B = 1$ MG, $V = 4 \times 10^{-4}$ deg/G/cm for 532 nm [25] and for $L = 0.05$ cm the Faraday rotation angle is $\alpha \sim 20°$. This is an easily detectable value. The relative change of the light intensity after the analyzer I/I_0 from Malus' law can be written as:

$$I/I_0 = [k + \sin^2(\alpha_0 + \alpha)]/[k + \sin^2(\alpha_0)], \qquad (5)$$

where k is polarimetry contrast ($k \sim 10^{-4}$), α_0 is the decrossing angle between the polarizer and the analyzer. For $I/I_0 = 1.1$ (10% change) and $\alpha_0 = 6°$ the detection threshold is $\alpha \sim 0.3°$. This gives an estimate of $\sim$15 kG for the minimum detectable magnetic field.

2. Kerr effect

The phase shift of a probe electromagnetic wave in the presence of a static electric field can be estimated as $\Delta\phi = 2\pi B_k E^2 L$. The Kerr constant B_k for SiO$_2$ is $\sim 10^{-13}$ cm/V^2 [26]. For silica glass, a breakdown electric field $E \sim 10^8$ V/cm, and a path length $L = 0.05$ cm, the phase shift for the probe beam equals $\Delta\phi \sim 100\pi$. This is a huge and a very easy detectable value of the phase shift. To determine the detection threshold, we will use a modified formula (3) from [23] for relative change of the light intensity I/I_0 after analyzer for the Kerr effect:

$$I/I_0 = [k + \sin^2(\alpha_0) - \sin 2(\alpha_0 - \alpha_E) \sin(2\alpha_E)$$
$$\times \sin^2(\Delta\phi/2)]/[k + \sin^2(\alpha_0)], \qquad (6)$$

where k is the polarimetry contrast ($k \sim 10^{-4}$), α_0 is the decrossing angle between the polarizer and the analyzer, α_E is the external electric field angle to the analyzer.

For $I/I_0 = 1.1$ (10% change), $\alpha_0 = 6°$ and $\alpha_E = 45°$ (maximum polarimeter sensitivity), the minimum phase shift equals $\Delta\phi = 0.01\pi$. In this case, the minimum detectable electric field is $\sim$1 MV/cm.

IV. THEORETICAL INTERPRETATION

A. Analytic estimate of the electron beam speed

The penetration of a fast electron beam into an insulating target can be considered as an ionization wave propagating with a constant velocity v_f. Ahead of the wave front the target is not ionized and the fast electrons rapidly slowdown in the self-consistent electric potential. Behind the ionization front, free electrons from target ionization appear. Their motion is able to neutralize the large electric field in that volume and allow the fast electrons to propagate through the plasma. Following [7], the penetration of the beam of hot electrons can be described in the reference frame of the ionization wave. To define the velocity of the ionization front one takes an electric field, E (sheath field) equal to the threshold for the field ionization of silica ($E_{th} \sim 10^{10}$ V/m in [28]). The electric field can be simply evaluated by considering electrons in the

front reference frame marked with a prime: $E \approx (8\pi n'_h T'_h)^{1/2}$, similar to the sheath field at the plasma vacuum interface [29]. Here n'_h and T'_h are the characteristic fast electron density and energy connected with corresponding values in the laboratory frame n_h and T_h through the Lorentz transform defined by the velocity (v_f) of the ionization front [7]. Then equation $(8\pi n'_h T'_h)^{1/2} = E_{th}$ becomes:

$$\beta_f \sqrt{\gamma^2 - 1} + \sqrt{1 - \beta_f^2} = \gamma - \frac{E_{th}^2}{8\pi n_h mc^2} \qquad (7)$$

where $\beta_f = v_f/c$ and γ defines a hot electron energy as $T_h = mc^2(\gamma - 1)$. Equation (7) defines ionization front velocity versus the hot electron energy, which can be explicitly represented as:

$$\beta_f = 1/\gamma^2 \left[\left(\gamma - \frac{E_{th}^2}{8\pi n_h mc^2} \right) \sqrt{\gamma^2 - 1} \right.$$
$$\left. + \sqrt{\gamma^2 - \left(\gamma - \frac{E_{th}^2}{8\pi n_h mc^2} \right)^2} \right] \qquad (8)$$

We use the ponderomotive scaling for hot electron energy from [30] $\gamma = (1 + a^2/2)^{1/2}$, where $a = 0.85(I_{18}\lambda^2)^{1/2}$, I_{18} denotes an absorbed laser intensity I in 10^{18} W/cm^2 units, and the laser wavelength λ is given in μm. Equation (8) gives the dependence $v_f(I)$.

At relativistic laser intensities, a considerable part of laser energy is absorbed. We define $I = AI_0$ with an absorption coefficient $A \sim (I_0)^{0.34}$ corresponding to $A = 90\%$ for a vacuum intensity $I_0 = 10^{21}$ W/cm^2. Such a dependence fits well the range measurements of total absorption of short laser pulses over a wide range of laser intensities for normal laser incident onto solid targets on the Callisto laser in the Jupiter laser facility at Lawrence Livermore National Laboratory for 10^{17} W/cm$^2 \leqslant I_0 \leqslant 3 \times 10^{20}$ W/cm^2 [31]. Typically, the threshold for field ionization is very low. This allows one to neglect $E_{th}^2/8\pi n_h mc^2$ in equation (8). In this case the dependence $v_f(I)$ is shown as a solid line in Fig. 7 and fits qualitatively well to available experimental data on ionization wave velocity for both low-flux and high-flux laser experiments.

B. PIC simulations of an earlier stage of electrons-glass interaction

The physics of an earlier stage of ionization wave driven by a relativistic electron current in an insulating target were modeled by PICLS [27], a 2-D, Cartesian particle-in-cell (PIC) code featuring binary collision and dynamic ionization. We used field ionization and the Thomas-Fermi (TF) ionization model for collisionally heated plasmas to calculate ionization levels. Using the TF model for the collisional ionization, the fast ionization waves are driven by the field ionization, so that the simulation results are insensitive to the TF model. The calculation is spatially resolved in the direction of laser propagation and in one dimension transverse to the laser.

This simulation of energy transport in a solid is rather demanding and cannot be performed on the ps time scale involved in the experiments. However, the aim of the PIC model is to clarify the ionization processes and to qualitatively confirm the trend of the observed phenomena after only

0.3-ps of simulation time and in a 100-μm by 75-μm simulation spatial domain. A single run of the simulation took approximately one week to generate the results presented herein. An experimental mm-scale simulation with the kinetic model is not realistic due to a limitation of computational resources of the NTF cluster.

The target consists of solid silica (SiO$_2$) arranged in slab geometry. A 5-μm length of low-density gas is placed in front of the target as a pre-plasma. The silica is composed of oxygen ($Z = 8$) and silicon ($Z = 14$) in a ratio of 2:1 with a corresponding ion density $n_O = 46n_c$ and $n_{Si} = 23n_c$, respectively, where $n_c = 10^{21}$ cm^{-3} is the electron's critical density for 1-μm laser light. The mass density of silica is set to 2.6 g/cm^3. Initially, the target was un-ionized with no free electrons. When fully ionized, the electron density could reach $n_e = 690n_c$. The simulation box is 75 μm $\times$ 100 μm containing 3000 $\times$ 4000 grid cells with each grid cell containing 6 "macro" ions and up to 60 electrons for total of 686 million particles. Each "macro" particle consists of $\sim 7 \times 10^{10}$ cm^{-1} (equivalent to 1.8 $\times$ 10^5 particles in 3D) ions or electrons, respectively. The driving-laser oscillation period is resolved by ~ 40 time steps. To avoid numerical heating and numerical ionization, we adopted 4th-order interpolation in the PIC calculations. As a result of the interpolative smoothing of the calculated fields, the numerical noise is damped and will be less than the breakdown field ($\sim 10^{10}$ V/m).

The laser parameters used in the simulation are based on the NTF, Leopard Laser parameters. The wavelength is set to 1 μm with a focal spot size of 10 μm. The pulse length is set to 500 fs with a 100-fs rise/fall time. The peak intensity is 5×10^{18} W/cm^2, corresponding to a normalized amplitude $a = eE/m_e c\omega \sim 2.2$ where m_e is the electron mass, c is the speed of light, and ω is the laser frequency. We have used absorbing boundaries for both electromagnetic waves and particles, which completely lose their energy when a boundary is encountered.

A snapshot of the 2D simulation at 300 fs is shown in Fig. 13. We find that two different electric fields are involved for relativistic laser-driven ionization and fast-electron transport in an insulator. The first is an electric sheath field, which exceeds the threshold for the field ionization of silica ($\sim 10^8$ V/cm [28]). The ionization wave front is seen in Fig. 13(a) at $x \sim 55$ μm. At $x > 55$ μm the target is not ionized and the fast electrons are slowing down in the self-consistent potential. Behind the ionization front, free electrons appear. Their motion suppresses the large electric field and allows the fast electrons to propagate through the plasma. The sheath field can be simply evaluated by considering electrons in the front reference frame $E \sim T'_h/e\lambda_{Dh} \sim (n'_h T'_h)^{1/2}$, similar to the sheath field at the plasma vacuum interface [29]. Here n'_h and T'_h are the characteristic fast-electron densities and energies (prime marks the front reference frame) connected with corresponding values in the laboratory frame through the Lorentz transform defined by the velocity (v_f) of the ionization front [7]. The hot-electron Debye length is given as λ_{Dh} and corresponds to the width of the sheath field (~ 5 μm). Most of the hot electrons are stopped and reflected back in this electrostatic potential $\Phi_s = eE\lambda_{Dh}$ as seen in Fig. 13(c). Note that there are filamentations of the ionization path as seen in Fig. 13(d) behind the ionization front as a result of the
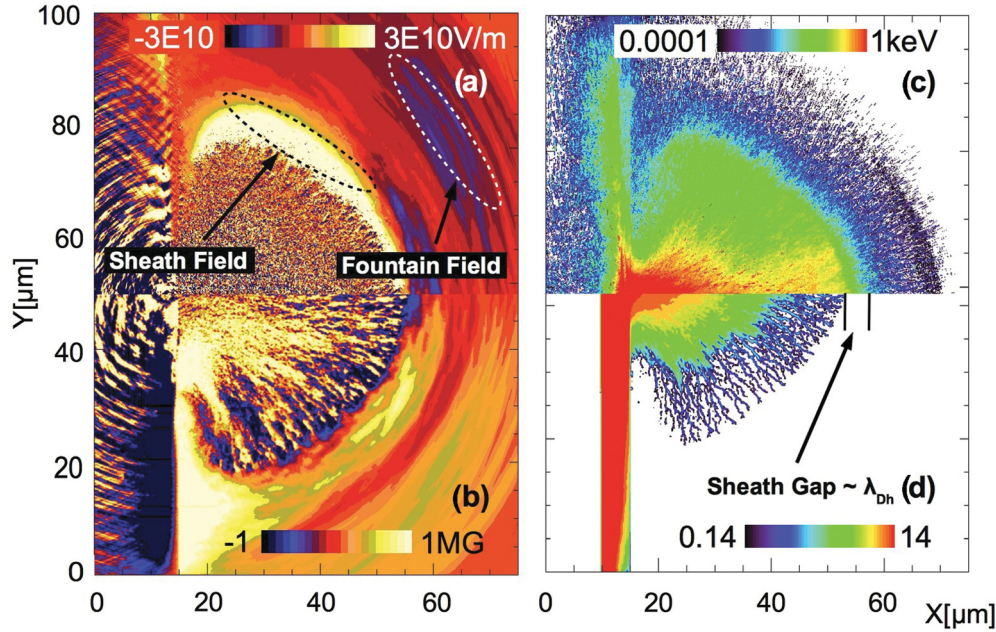
FIG. 13. (Color online) 2D spatial PIC results are shown at $t = 300$ fs: (a) the lateral electric field E_y, (b) the quasi-static magnetic field B_z, (c) the electron energy density, and (d) the ionization level of the silicon are presented.

breakdown processes, like lightning in sky, and these filaments, in return, cause the magnetic filamentations shown in Fig. 13(b).

The second electric field is driven by fast electrons with energies above $e\Phi_s$, which travel through the potential gap and form a fast-electron cloud layer on top of the ionization front, as in Fig. 13(c). Our calculations gave a temperature of ~500 keV with electron energies up to 5 MeV. The absence of free electrons in insulators precludes the possibility of a neutralizing return current. As a consequence, these electrons carry net charge and current, and they excite the lateral electrostatic field located beyond the ionization front, marked as "fountain field" in Fig. 13(a). Since this electric field is weaker than E_b, no breakdown occurs, but fast electrons diverge laterally and turn around by this self induced field, like a "fountain" of electrons. The corresponding azimuthal magnetic field (~500 kG), Fig. 13(b), is also excited by lateral electron motion. We call this motion pattern the "fountain effect". The electric field component of the electron fountain is purely radial (E_y) because the longitudinal component is of negligible magnitude. The Larmor radii of a few-MeV electrons in this magnetic field are about a few hundred microns. The transverse push by E_y also takes a few hundred microns to turn the direction of a MeV electron. This exceeds the simulation box and, thus, the actual fountain motion cannot be explicitly shown due to limitation in computational space.

Additional 1D PICLS simulations have revealed that the ionization front continues to propagate well after the laser beam cuts off. Although the speed of propagation depends on the fast electron energies, the ionization field geometry does not. It depends on the number of electrons ahead of the wave. Since the fast electrons continue to propagate in the material regardless of whether the laser pulse is turned on or off, this maintains the sheath field long after the pulse is gone. Figure 14 demonstrates this effect (no recombination taken

into account). As with the simulation in the paper, a 500-fs laser pulse is used. Our interferometric data at 1.7 ps and 3.3 ps (Fig. 10) showed a significantly smaller electron density by ~3 orders of magnitude. A noted discrepancy in electron densities between the experiments and the simulations can be attributed to collisional 3-body recombination, whose rates are estimated to be around 7×10^{14} s^{-1} for a 10-eV plasma. These 3-body rates are not used in the simulation. This recombination rate should reduce plasma density significantly over ps time scales.

Note here that the simulated propagation speed of the ionization wave, 20-30% of the speed of light, is consistent with the experimental observation $\sim c/3$. Because the sheath
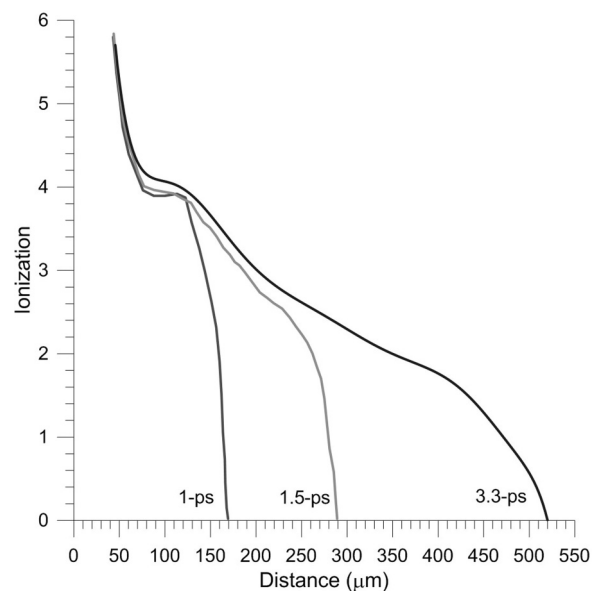
FIG. 14. 1D simulations of ionization vs. distance are plotted for $t = 1$, 1.5 and 3.3 ps.

field of breakdown does not depend on electron energy but the number of electrons in front of the wave, the breakdown will continuously propagate long after the laser pulse is turned off as seen in Fig. 4.

V. CONCLUSION

In summary, laser probe diagnostics—shadowgraphy, interferometry, and polarimetry—were used to comprehensively characterize the ionization-wave dynamics induced by a laser-driven, relativistic electron beam inside a glass target. For a laser flux $\sim 2 \times 10^{18}$ W/cm^2 the ionization wave propagates $\sim 750\,\mu$m during first ~ 10 ps with maximum speed $\sim c/3$. The dynamics of the ionization wave inside the glass target is in a reasonable agreement to measurements in other publications [13,14]. The maximum of the free-electron density inside glass target was $\sim 2 \times 10^{19}$ cm^{-3}, which corresponds to an ionization level of $\sim 0.1\%$. The magnetic fields and electric fields did not exceed ~ 15 kG and ~ 1 MV/cm (1/100 of breakdown field in glass), respectively. The electron temperature had a hot ringlike structure with a maximum average temperature of ~ 0.7 eV. The topology of the interference

phase shift showed the characteristic feature of the fountain effect, a narrow electron beam that fanned out away from the propagation axis and returned back to the target surface. The very low ionization level, $\sim 0.1\%$, observed after the end of the heating pulse suggested fast recombination occurring on a sub-ps time scale.

Two-dimensional PIC simulations showed the dynamics of an ionization wave during the heating time in the breakdown regime driven by a relativistic electron current and suggested the existence of a fountain of fast electrons in front of the ionization wave. A strong modulation was observed in the simulations behind the ionization front due to breakdown processes. Filaments of MG magnetic fields were also seen and fast electron flow was modulated in the transport, which is consistent with previous observations [32].

[1] G. Malka and J. L. Miquel, Phys. Rev. Lett. **77**, 75 (1996); W. Yu, V. Bychenkov, Y. Sentoku, M. Y. Yu, Z. M. Sheng, and K. Mima, *ibid*. **85**, 570 (2000); T. Katsouleas, Nature (London) **444**, 688 (2006); A. G. Mordovanakis *et al*., Phys. Rev. Lett. **103**, 235001 (2009).

[2] N. G. Basov, S. Y. Guskov, and L. P. Feoktistov, J. Sov. Laser Res. **13**, 396 (1992); M. Tabak *et al*., Phys. Plasmas **1**, 1626 (1994).

[3] W. Theobald *et al*., Phys. Plasmas **13**, 043102 (2006).

[4] P. A. Norreys *et al*., Phys. Plasmas **6**, 2150 (1999).

[5] A. R. Bell, J. R. Davies, S. Guerin, and H. Ruhl, Plasma Phys. Controlled Fusion **39**, 653 (1997).

[6] J. R. Davies, A. R. Bell, M. G. Haines, and S. M. Guerin, Phys. Rev. E **56**, 7193 (1997).

[7] A. Debayle and V. T. Tikhonchuk, Phys. Plasmas **14**, 073104 (2007).

[8] Y. Sentoku *et al*., Appl. Phys. B **74**, 207 (2002).

[9] M. H. Key *et al*., Phys. Plasmas **5**, 1966 (1998).

[10] K. B. Wharton, S. P. Hatchett, S. C. Wilks, M. H. Key, J. D. Moody, V. Yanovsky, A. A. Offenberger, B. A. Hammel, M. D. Perry, and C. Joshi, Phys. Rev. Lett. **81**, 822 (1998).

[11] F. Pisani *et al*., Phys. Rev. E **62**, R5927 (2000).

[12] B. T. V. Vu, A. Szoke, and O. L. Landen, Phys. Rev. Lett. **72**, 3823 (1994).

[13] T. Ditmire, E. T. Gumbrell, R. A. Smith, L. Mountford, and M. H. R. Hutchinson, Phys. Rev. Lett. **77**, 498 (1996); E. T. Gumbrell *et al*., Phys. Plasma **5**, 3714 (1998).

[14] L. Gremillet *et al*., Phys. Rev. Lett. **83**, 5015 (1999).

[15] A. J. Kemp, Y. Sentoku, T. Cowan, and J. Fuchs, Phys. Plasma **10**, L69 (2004).

[16] G. S. Sarkisov *et al*., Appl. Phys. Lett. **99**, 131501 (2011).

[17] P. P. Wiewior, V. V. Ivanov, and O. Chalyy, J. Phys.: Conf. Ser. **244**, 032013 (2010).

[18] G. S. Sarkisov, Instrum. Exp. Tech. **39**, 727 (1996); http://en.wikipedia.org/wiki/Air-wedge_shearing_interferometer

[19] G. S. Sarkisov, V. Y. Bychenkov, V. N. Novikov, V. T. Tikhonchuk, A. Maksimchuk, S. Y. Chen, R. Wagner, G. Mourou, and D. Umstadter, Phys. Rev. E **59**, 7042 (1999); G. S. Sarkisov, I. L. Beigman, V. P. Shevelko, and K. W. Struve, Phys. Rev. A **73**, 042501 (2006).

[20] G. S. Sarkisov and B. Etlicher, JETP Lett. **62**, 797 (1995).

[21] J. F. Williams and L. J. Allen, J. Phys. B **22**, 3529 (1989).

[22] G. S. Sarkisov and J. R. Woodworth, J Appl. Phys. **99**, 093307 (2006).

[23] G. S. Sarkisov, N. D. Zameroski, and J. R. Woodworth, J Appl. Phys. **99**, 083304 (2006).

[24] T. Pisarzyk, A. A. Rupasov, G. S. Sarkisov, and A. S. Shikanov, J. Sov. Laser Research **11**, 1 (1990).

[25] A. Jain, J. Kumar, F. Zhou, L. Li, and S. Tripathy, Am. J. Phys. **67**, 714 (1998).

[26] N. F. Borrelli, Phys. Chem. Glass **12**, 93 (1971).

[27] Y. Sentoku and A. J. Kemp, J. Comp. Phys. **227**, 6846 (2008).

[28] D. von der Linde and H. Schuler, J. Opt. Soc. Am. B **13**, 216 (1996).

[29] V. Yu. Bychenkov *et al*., Phys. Plasma **11**, 3242 (2004).

[30] S. C. Wilks, W. L. Kruer, M. Tabak, and A. B. Langdon, Phys. Rev. Lett. **69**, 1383 (1992).

[31] Y. Ping *et al*., Phys. Rev. Lett. **100**, 085004 (2008).

[32] J. Fuchs *et al*., Phys. Rev. Lett. **91**, 255002 (2003).